Journal of Colloid and Interface Science 584 (2021) 582–591

Contents lists available at ScienceDirect

Journal of Colloid and Interface Science

journal homepage: www.elsevier.com/locate/jcis

Regular Article

pn-Heterojunction of the SWCNT/ZnO nanocomposite for temperature dependent reaction with hydrogen

Nguyen Duc Chinh [a], Yang Haneul [a], Nguyen Minh Hieu [a], Nguyen Manh Hung [a,b], Nguyen Duc Quang [a], Chunjoong Kim [a,*], Dojin Kim [a,*]

[a] Department of Materials Science and Engineering, Chungnam National University, Daejeon, 34134, Republic of Korea
[b] Department of Materials Science and Engineering, Le Quy Don Technical University, Hanoi, 100000, Vietnam

HIGHLIGHTS

- *pn* Junction type nanocomposite sensors of SWCNT/ZnO for hydrogen sensing.
- The composite responded to ppm levels of H_2 andexhibited the highest response at RT.
- The mechanism of enhanced H2 response in the composite sensor at RT was elaborated.
- Our results pave the way to build a portable and low-powered device for H_2 breath test.

GRAPHICAL ABSTRACT

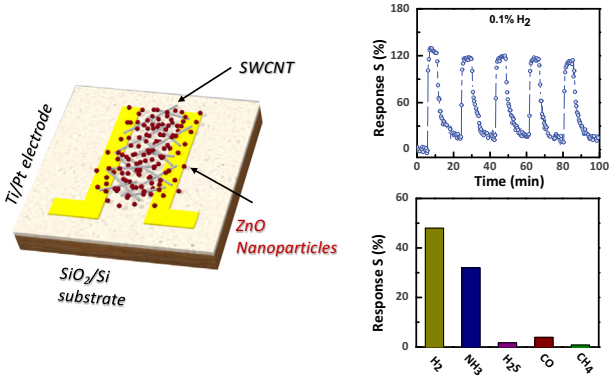

ARTICLE INFO

Article history:
Received 5 October 2020
Accepted 5 October 2020
Available online 13 October 2020

Keywords:
Hydrogen sensing
Breath tests
Room-temperature sensing
SWCNT/ZnO nanocomposite

ABSTRACT

A hydrogen breath test is a non-invasive and safe diagnostic tool to explore the functional gastrointestinal disorders. For the diagnosis of small intestinal bacterial overgrowth syndrome as well as carbohydrate malabsorption such as fructose, lactose, and sorbitol malabsorption, a hydrogen breath test is considered one of the gold criterions. Since the more sensitive hydrogen sensor enables the more accurate prediction about the disease, many efforts have been to the development of the high performance H_2 sensor. Herein, we fabricate the *pn*-junction type composite sensors using single wall carbon nanotube (SWCNT) and zinc oxide and thoroughly investigate their hydrogen sensing properties at various temperatures. We discuss the origin of sensing performance enhancement mechanism in the composite sensors, while the composite sensor with high H_2 sensing performance, linearity, repeatability, and selectivity can be prepared.

1. Introduction

Over the last decades, the breath analysis for the routine monitoring of halitosis, metabolism, and disease is of scientific interest since breath sampling is non-invasive, painless, and acceptable to patients. The analysis of exhaled breath has been proposed as a convenient and safe diagnosis complementary to blood and urine sampling [1,2]. The main composition of human exhaled breath consists of nitrogen that is most common in the atmosphere, carbon dioxide produced by respiration, oxygen that is inhaled but not consumed, and water vapour generated from bodily fluids. In

* Corresponding authors.
E-mail addresses: ckim0218@cnu.ac.kr (C. Kim), dojin@cnu.ac.kr (D. Kim).

https://doi.org/10.1016/j.jcis.2020.10.017
0021-9797/

addition, more than 500 kinds of gas components with less than 100 ppm (parts per million) comprise an exhaled breath, which include carbon monoxide, methane, hydrogen and numerous volatile organic compounds (VOC) [3–6]. The components and concentration of certain gases in exhaled breath have been regarded as biomarkers for the specific diseases. Therefore, sensors that can respond very low amount of gaseous components enable analysis of human breath and thus their health state.

Recently, hydrogen has attracted great attraction in the health care as well as in the industry. Ohsawa *et al.* reported that hydrogen can reduce the cytotoxic oxygen radical, which is considered harmful in high concentration [7]. In the human body, hydrogen is produced by bacteria in the intestinal environment [8,9]. Anaerobic bacteria prefer to metabolize sugar molecules as part of the fermentation reaction [10]. When nutrients are not absorbed in the small intestine, they directly enter into the large intestine, by which the bacteria grow in large amounts and produce abundant gas including hydrogen, methane, carbon dioxide, etc [11]. Thus, monitoring of hydrogen level can be used as a gauge to examine the intestinal condition. For the diagnosis of small intestinal bacterial overgrowth syndrome as well as carbohydrate malabsorption such as fructose, lactose, and sorbitol malabsorption, a hydrogen breath test has been widely used. In order to diagnosis the human health more accurately, sensors with high performance and stability should be made in urgent manner.

The sensing materials are the key components in chemical sensors. During the last decade, carbon nanotubes (CNTs) have been considered ideal sensing materials for chemical sensors because of their unique properties. Single-walled carbon nanotubes (SWCNTs) have exhibited a sensitivity by charge exchange with their chemical environment since they are almost entirely composed of surface atoms and are very sensitive toward adsorbates [12–15]. SWCNTs possess high aspect ratio, good environmental stability, excellent mechanical and electronic properties, and ultrahigh surface to volume ratios, making them attractive for chemical sensing applications. Furthermore, SWCNT sensors can work even at room temperature (RT) operation and allows easy miniaturization of the sensor structure for massive sensor arrays. However, pristine SWCNTs showed weak responses and low selectivity toward specific gas molecules due to the weak interaction between SWCNTs and analyte molecules, thus SWCNTs should be functionalized to enhance both the sensitivity and the selectivity [16–20].

Sensors with *pn*-junction structure are reported to reveal the unique properties compared with n- or p-type sensors. The electronic system of different materials in contact is called heterojunction structure or heterostructure, which mostly comprises free carrier depleted interface regions due to the Fermi levels alignment process in thermal equilibrium [21]. Therefore, when current flows in this structure, the conductance of the heterostructure is not an arithmetic sum of the conductance of each layer due to the carrier-depleted junction region. In often times, the resulting conductance of the sensor system is reported to be advantageous to the enhancement of gas-sensing performance [22–24].

Herein, we reported about the SWCNT/ZnO pn-junction which showed different temperature dependent hydrogen detection properties depending on the volume ratio of SWCNT and ZnO. The SWCNT-dominated nanocomposite structure showed the high H_2 sensing performance at room temperature while the ZnO-dominated nanocomposite structure showed the high H_2 sensing performance at the elevated temperature. Thus, we for the first time systematically examined the effect of the pn-junction in the chemoresistive sensor structures and clarified the role of the junction for the sensor performance. We believe that our work provides the new composite chemical sensor for H_2 detection as well as the guide rule to exploit the sensing mechanism.

2. Experimental section

2.1. Fabrication of SWCNT/ZnO composite

Silicon substrates (SiO_2/Si, 5 mm × 5 mm × 0.65 mm, oxide thickness: 300 nm) were ultrasonically cleaned in the sequence of acetone, methanol, and deionized water for 15 min each followed by blow-drying with nitrogen gas. Titanium (30 nm) and platinum (120 nm) were sequentially deposited as an adhesion layer and a current collector, respectively, onto the substrate using a DC magnetron sputter through a shadow mask with the comb-type interdigitated pattern. The electrode-patterned substrates were mounted on the inside wall of the arc-discharge chamber as schematically shown in our previous reports [25,26]. Then, the SWCNTs network as the transducer of the sensor, by which the charge transport can be measured, was fabricated by an arc-discharge system. The active sensor area for SWCNTs deposition was defined by scotch-tape masking of the unwanted deposition area. The synthesis of SWCNTs network was carried out in an optimized condition of an arc current density of 40 A cm^{-2} in a hydrogen atmosphere with a partial pressure of 5.3 × 10^3 Pa for 5 s. A hollow pure graphite tube with a length of 160 mm, the outer diameter of 6.4 mm, and the inner diameter of 3 mm inserted with catalyst wires of Ni, Fe, and Mo were used as the carbon source for the arc discharge. The SWCNTs were directly deposited on the substrate while drifting in the chamber to the wall. The as-deposited SWCNTs were methanol-treated by dipping in methanol solution to enhance the adhesion of the SWCNTs on the SiO_2 substrate, thus the SWCNT network on the Si substrate with good mechanical contact could be formed. The substrate was then dried at 100 °C for 15 min. Finally, the SWCNT structure was heat-treated at 400 °C in the air for 2 h to remove amorphous carbon residual in the SWCNTs network [26,27]. This as-fabricated SWCNT sensor is labelled as C0.

Zinc (Zn) metal layers were deposited onto the SWCNTs network by a DC magnetron sputtering system. The deposition was performed at RT in Ar atmosphere with the working pressure and power of 5.0 × 10^{-3} Torr and 10 W, respectively. Various Zn deposition times were employed to vary the Zn thickness. 5, 15, 30, 60, 90, and 120 s-deposited on the SWCNTs network were labelled as ZC5, ZC15, ZC30, ZC60, ZC90, and ZC120, respectively. In addition, a pure Zn thin film sensor (Z0) was fabricated by the deposition of Zn on the SiO_2 substrate for 120 s for the comparison. The Zn-SWCNTs composite structures and a pure Zn film were heat-treated at 400 °C for 3 h in air to oxidize Zn to ZnO, resulting in formation of SWCNT/ZnO composite sensor structures. The flowchart for fabrication of the SWCNT/ZnO composite sensor structures with various ZnO contents is displayed in Fig. 1.

2.2. Structural characterization

The surface morphology and crystal structure of the SWCNT/ZnO network structures was investigated by field-emission scanning electron microscopy (FE-SEM; JSM 700F; JEOL, Japan), field-emission transmission electron microscopy (FE-TEM, Tecnai G^2 F30 S-TWIN, FEI, Netherlands), and X-ray diffraction (XRD; X'pert PRO-MPD, PANalytical, Netherlands) using Cu Kα radiation. The chemical bonding states were examined using X-ray photoelectron spectroscopy (XPS; Thermo Scientific MultiLab 2000 spectrometer, Pittsburgh, PA, USA) using monochromatic Al Kα, and Raman spectroscopy (UniRAM spectrometer with an excitation line at 532 nm and cooled CCD detector).

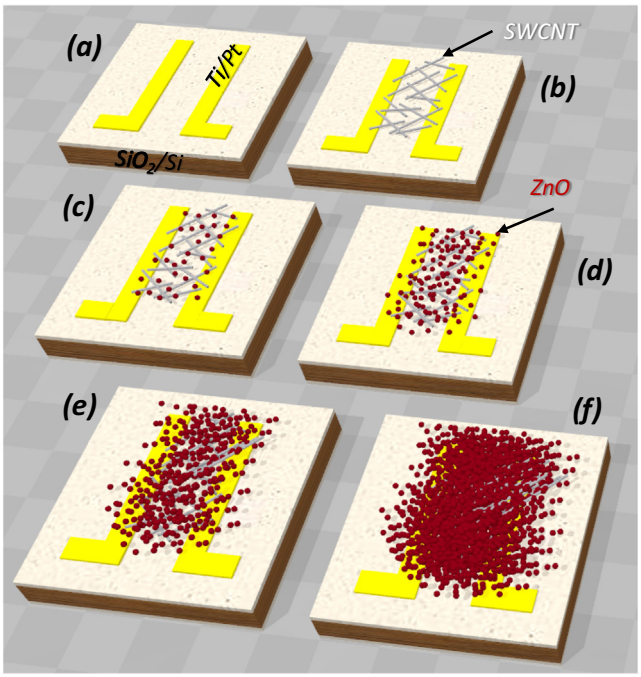

Fig. 1. The scheme about the fabrication of the SWCNT/ZnO composite sensors with different sputtering time of Zn.

2.3. Sensing property measurement

The schematic diagram of the setup for sensing property measurement is shown in Fig. 2. The nanostructure sensor devices were mounted in a test chamber in which the temperature and gas flow can be controlled. The analyte gases used (H_2, NH_3, H_2S, CH_4, and CO) are diluted in nitrogen; H_2 (5%), NH_3 (1000 ppm), H_2S (1000 ppm), CO (5%), and CH_4 (1%). The gas flow rate can be precisely controlled by the mass flow controllers (MFCs). The gas concentration, C (ppm), was determined using the relationship of C (ppm) = C_{std} (ppm) × f / (f + F), where f and F are the flow rates of the analyte gas and carrier gas (dry air), respectively, and C_{std} (ppm) is the analyte gas concentration in the cylinder. The current–voltage (I-V) characteristics were measured using a picoammeter/voltage source (Keithley 6487) and translated to the electrical gas sensing signals. The response of the sensor, S (%), is defined by $(G_o\text{-}G_g)/G_o \times 100$, where G_o is the standby conductance measured in dry air before exposure to the analyte gases and G_g is the conductance measured upon exposure to the analyte gases. The conductance data was calculated via the relationship $V = I/G$. We used conductance rather than resistance because the pn heterojunction formed in the sensor structure is presented by an equivalent circuit of parallel conductances. For investigation of the humidity effect, the relative humidity (RH) in the chamber was controlled by a bubbler system at 30 °C, and was measured by a humidity sensor (Testo 635, Germany) mounted in the test chamber.

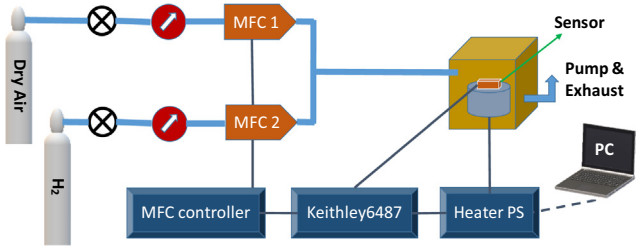

Fig. 2. Experimental set up for the measurement of hydrogen gas sensing properties.

3. Results and discussion

3.1. Morphology and structure characterization

SEM images of the fabricated SWCNT/ZnO network structures are presented in Fig. 3a–c for the different content of ZnO. The thickness of the SWCNT network is not thick enough to cover the whole substrate including the Pt electrode as can be seen by exposure of the bare substrate among the SWCNT network (Fig. 3a). Also, ZnO did not form conformal layer on the SWCNTs, rather ZnO islands preferentially grew along the nanotube bundles during heat-treatment. Up to the deposition time of 30 s, the electrode was not fully covered, as shown in Fig. 3b, but ZnO nanoparticles could completely cover the SWCNTs as well as the electrode after 90 s deposition, as shown in Fig. 3c. The ZnO nanoparticle size is less than ~ 100 nm. Additionally, Fig. 3d and 3e show low and high magnification TEM images, respectively, of the SWCNT/ZnO composite (ZC30), which further confirms homogeneous distribution of ZnO nanoparticles over the SWCNT. The SWCNTs with diameters from 5 to 10 nm were entangled with ~ 10 nm-sized ZnO nanoparticles. The lattice fringes corresponding to the spacing of 2.8 Å, 2.6 Å, and 2.47 Å match the (100), (002), and (101) planes of wurtzite zinc oxide (JCPDS, #36–1451), respectively. The XRD pattern of the SWCNT/ZnO composite is shown in Fig. 3f together with pure SWCNTs and ZnO structures. The peaks at 26.5° and 43° correspond to (002) and (100) lattice planes of SWCNTs, respectively (JCPDS, #75–1621) while the peaks at 32°, 34.5°, 36.4°, 47.7°, 56.8°, 63°, 68.1° correspond to (100), (002), (101), (102), (110), (103), and (112) of lattice planes of ZnO with wurtzite structure, respectively. It is obvious that crystalline phases of SWCNT and ZnO form in the ZnO/SWCNTs nanocomposite.

The X-ray photoelectron spectroscopy, Fig. 4a–c, was investigated to analyze the chemical bonds in the SWCNT/ZnO network. The core level spectra of the C *1s* state were composed of several characteristic peaks: the carbon–carbon interactions including C—C sp^2 bond at the binding energy of 284.5 eV, a relatively weak peak due to carbon–oxygen interactions including C—O bonds at 286.6 eV [28], and the π-π* satellite peak at 289.6 eV [29], as can be seen in Fig. 4a. The feature of the π-π* is the result of a mixture of interband transitions from π to π* and a π band plasmonic excitation, commonly seen in the C *1s* XPS spectra for graphene [30]. Fig. 4b shows the two peaks at binding energies of 1021.8 eV and 1044.8 eV in the XPS spectra of Zn *2p* and correspond to the Zn^{2+} $2p_{3/2}$ and Zn^{2+} $2p_{1/2}$, respectively [31,32]. The spectra for O *1s* shown in Fig. 4c indicates the binding energy of 530.6 eV that is attributed to O^{2-} ions on wurtzite structure of hexagonal Zn^{2+} ion array [33], of which strong feature indicates the oxygen to be fully oxidized by stoichiometric surrounding by Zn.

Raman spectroscopy was analyzed to characterize the quality of carbon nanotubes. The Raman spectrum of SWCNTs, Fig. 4d, typically consists of two major peaks at ~ 1340 cm^{-1} and ~ 1595 cm^{-1}, which are originated from D- and G-bands, respectively [34]. The D-band induced by sp^3 electronic states is known to be associated with defective, disordered graphite or glassy carbon, while the G-band is related to the sp^2 vibration of a two-dimensional hexagonal lattice in the graphite. This mode reflects the structural integrity of sp^2-hybridised carbon atoms of the SWCNTs. The very high G-band peak intensity compared with the D-band is a typical feature of the SWCNTs with high crystalline quality [35]. The very high ratio of the G-band to the D-band peak intensities of SWCNTs (I_D/I_G) was observed to be ~ 6, indicating the high quality of the

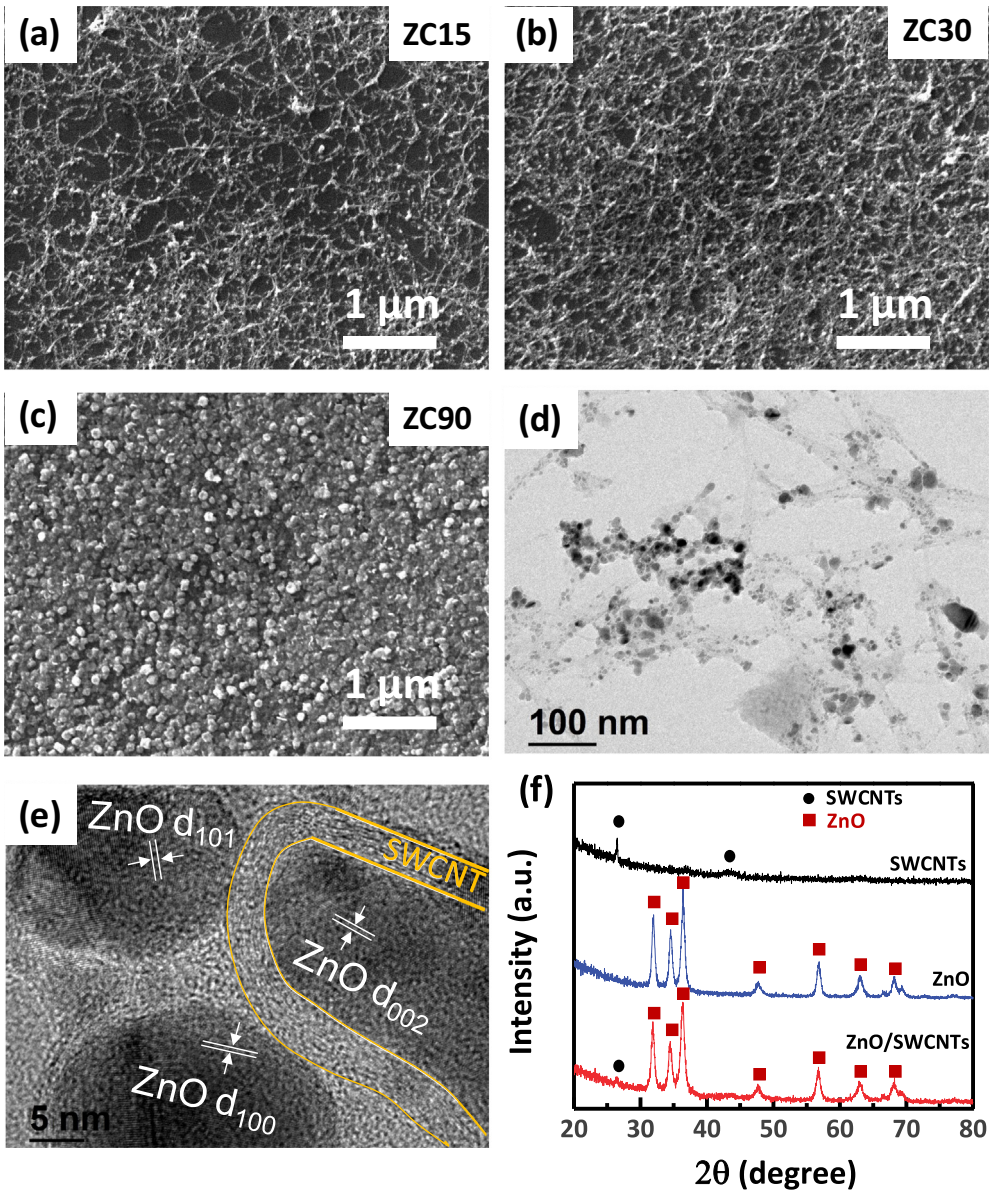

Fig. 3. SEM images of SWCNT/ZnO composites of (a) ZC15, (b) ZC30, and (c) ZC90. TEM images of the SWCNT/ZnO composite (ZC30) with (d) low and (e) high magnification. (f) XRD patterns of pure-SWCNTs, SWCNT/ZnO composite, and pure-ZnO.

as-fabricated SWCNTs. The spectrum was normalized to the G' band at ~ 2650 cm-1 (now shown in the Fig. 4d), which does not depend on defect concentration [36]. Meanwhile, the decrease in the ratio of G/D band peaks in the SWCNT/ZnO composite results from the formation of defects in the SWCNTs via sputtering process of ZnO.

3.2. Electrical properties

The current–voltage (*I-V*) characteristics for SWCNTs, ZnO, and SWCNT/ZnO composites were measured at room temperature (RT; 30 °C). Prior to the measurement, all samples were heated at 350 °C in dry air ambient to desorb the water molecules from the surface and cooled down to RT. As shown in Fig. 5a, all structures showed good ohmic behaviours, which were plotted in logarithmic scale due to five orders of magnitude difference in the current among the sensors. Then, the conductance of the sensor structures were measured with elevating temperature from 30 °C to 350 °C in dry air (Fig. 5b and c).

The Arrhenius plot between temperature and conductance (G), Fig. 5b, supports a thermally activated process for the conductance [$G \propto \exp(-\Delta E/k_B T)$] owing to the thermal ionization of electron or hole carriers in the semiconductor materials. The slope of the curves attributed to the activation energy (ΔE) for the conduction can be distinguished into two groups. One group shows ΔE of ~ 0.05 eV for C0 (SWCNTs), ZC5, ZC15, ZC30, and ZC60. Whereas ΔE of the other group, ZC90, ZC120, and Z0 (ZnO), is ~ 0.26 eV. The former and the latter sensor group can be labelled as '*SWCNT-dominated*' and '*ZnO-dominated*', respectively, because sensors in the former and the latter group follow the characteristics of p-type SWCNT and *n*-type ZnO, respectively, as discussed later. It should be noted that SWCNT is a p-type semiconductor with high conductivity [37–39], and ZnO is an *n*-type semiconductor with wide bandgap energy of 3.3 eV [40]. Indeed, higher activation energies for conduction in the ZnO dominated sensors could be observed compared with those in the SWCNT dominated sensors (Fig. 5b). In other word, ZnO dominated sensors reveal lower

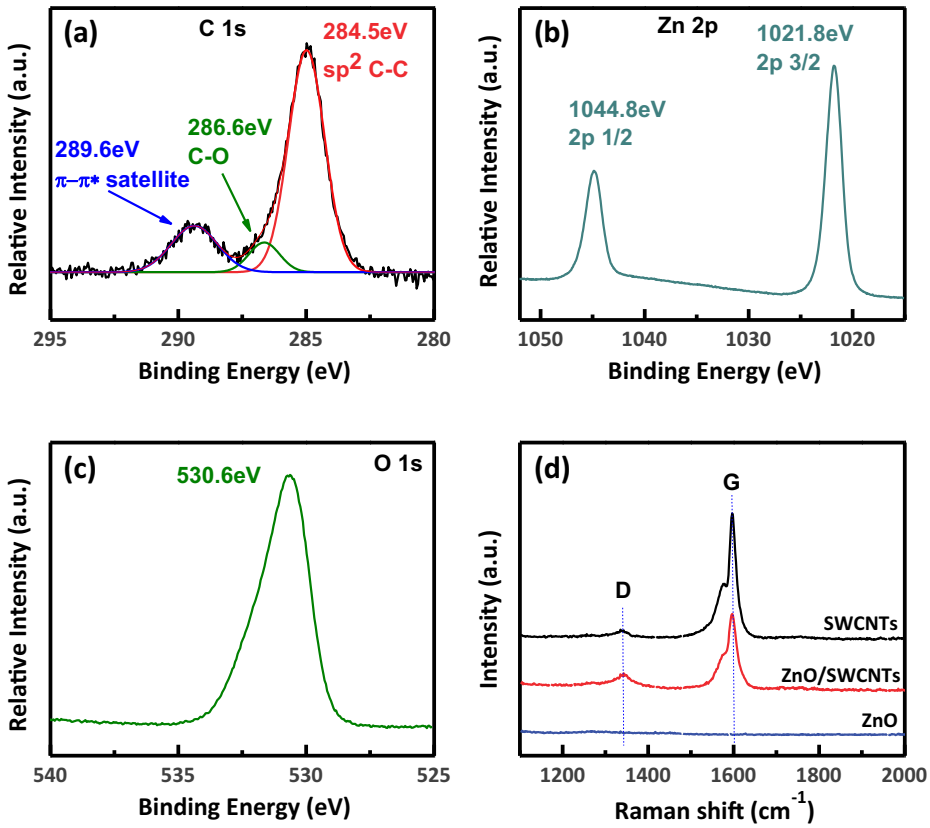

Fig. 4. XPS spectra of (a) C 1s, (b) Zn 2p, and (c) O 1s states of the SWCNT/ZnO composite (ZC30) and (d) Raman spectra of the as-fabricated SWCNTs, SWCNT/ZnO composite, and ZnO.

conductivity than SWCNT dominated sensors due to the semi-metallic SWCNT and semiconducting ZnO nature.

The temperature dependent conductance of the structures was replotted in Fig. 5c to systematically study the effect of ZnO content on the conductance. It clearly shows that conductance is in inverse proportion to the content of ZnO until 90 s deposition of ZnO (ZC90) regardless of the sensor temperature. However, the conductance increases if thicker ZnO is deposited on SWCNTs such as ZC120 and Z0. The conductance variation of the sensors by Zn sputtering time (or thickness of ZnO) can be explained through the schematics shown in the left panel of Fig. 6. We should recall that ZnO is preferentially formed by the islands of nanoparticles as shown in Fig. 3. The depletion region formed at the contact is practically insulating, therefore rendering the conductance of the materials decreased. As more and larger ZnO nanoparticles grow on the SWCNT network, the increasing contact area between SWCNT and ZnO further decrease the conductance.

The conductance was highest with C0 (SWCNT) among the sensors, however, it decreased by five orders of magnitude till deposition of ZnO for 90 s. The increase in number and size of ZnO accounts for larger contact area between SWCNTs and ZnO followed by the increase in the depletion region of SWCNTs. The surface of the SWCNT can adsorb oxygen from the environment and such condition is assumed to be maintained at an elevated temperature. The schematic about the SWCNT with oxygen adsorption is presented in Fig. 6**a**. The ZnO nanoparticles also can adsorb oxygen molecules at RT and the surface of ZnO is depleted of electrons as much as adsorbed oxygen. When the ZnO nanoparticle contacts with SWCNTs, the ZnO particle is further depleted of electrons via formation of pn-junction. For small ZnO particles, the pn junction formation can completely deplete the whole particle. The concomitant depletion of holes at the SWCNT side of pn-junction leads to the decrease in the conductance of the SWCNT transducer. The schematic for ZC5 in Fig. 6**b** illustrated this condition that all ZnO particles are in contact with the SWCNT under complete depletion of electrons and the current is comprised by only hole transport via the SWCNT. Therefore, the conduction in the ZC5 sensor can be achieved through the hole transport like a p-type conductor. As the number and size of ZnO particles increase, the area of pn-junction continues to increase, which results in the decrease in conductance of the SWCNT until ZC60. We will discuss later that the maximum response is observed in ZC30 with an intermediate ZnO coverage (Fig. 5c and Fig. 6**c**).

Further deposition of ZnO nanoparticles renders the whole SWCNT network completely depleted while excess ZnO nanoparticles do not participate in the pn-junction formation, leading to the conduction type conversion. Considering the initial morphology of the SWCNTs on the substrate with low density (Fig. 3a), the stacking of ZnO particles over the network will completely deplete the SWCNTs while the free-of-contact ZnO particles possess *n*-type neutral region. In this criterion, SWCNTs are insulating and the current flows via electron transport through the ZnO nanoparticles, leading to the *n*-type conduction, which matches the case of ZC90 (Fig. 5 and Fig. 6**d**). Therefore, the minimum conductance of the nanocomposite sensor due to the maximum depletion layer volume ratio is considered between ZC60 and ZC90. The ZC120 composite, more *n*-type conducting mechanism works with greater ZnO volume albeit less than pure ZnO (Z0). The transition of conduction type from hole transport to electron transport by deposition of ZnO corroborate the classification of '*SWCNT-dominated*' and '*ZnO-dominated*' sensors, which was derived from the difference in the thermal activation energy for free carriers' conduction. The discussion above will be further confirmed by the measurement of sensing property (**Fig. S1**).

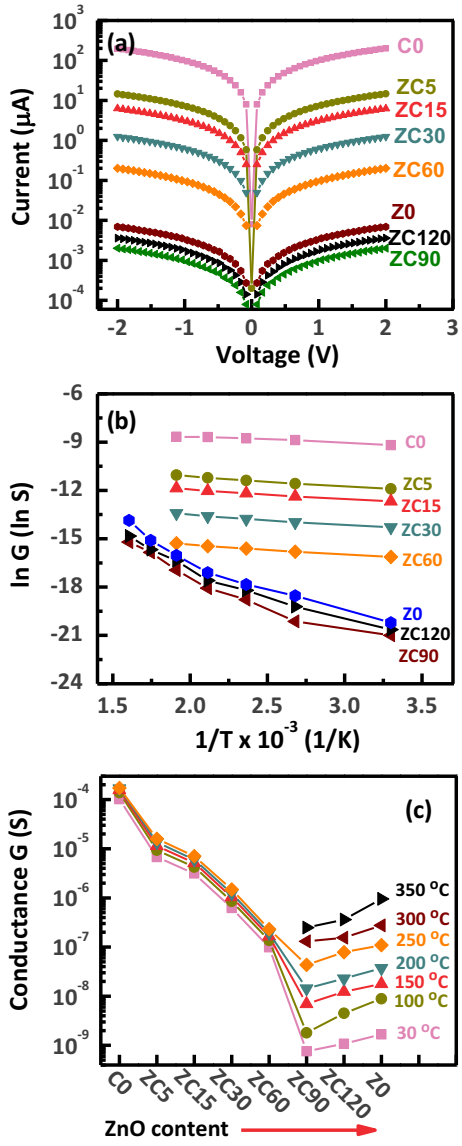

Fig. 5. (a) Current-voltage (I-V) characteristics of the SWCNT/ZnO composite sensors at RT (30 °C). The temperature dependence of the conductance (G) of the sensors is shown as a function of (b) temperature and (c) ZnO content.

3.3. Hydrogen gas sensing properties

H_2 sensing properties of the sensors were examined at various working temperatures from RT to 350 °C. Response and recovery were measured upon exposure to 500 ppm H_2 diluted in dry air as shown in **Fig. S1**. Considering the sensor response, $S=(G_o-G_g)/G_o \times 100$, the sensing behaviors can be categorized by two groups: the positive response group (**Fig. S1a-S1e** for C0 and ZC5 to ZC60) and the negative response group (**Fig. S1f-S1h** for ZC90, ZC120, and Z0). The sensing polarity is originated from the major charge carrier types; the former group is *SWCNT-dominated* (*p*-type) and the latter group is *ZnO-dominated* (*n*-type). The SWCNT-dominated sensors revealed the maximum response at room temperature with the ZC30. On the other hand, the ZnO-dominated sensors revealed the maximum response at 250 °C with the pure ZnO film (Z0). These results proved that the sensing mechanism of the SWCNT-dominated and ZnO-dominated sensors followed that of SWCNT and ZnO, respectively [21].

The conductance change of the sensors for different operating temperatures are plotted in Fig. 7a. The response levels of sensors at various temperatures are summarized in Fig. 7b, while response levels as the content of ZnO in the composite are presented in Fig. 7c. The response was highest at RT and degraded at higher temperature in C0 (pure SWCNT), however, Z0 (pure ZnO) showed the highest response at 250 °C but no response at RT. As shown in Fig. 7c, SWCNT (C0) and ZnO (Z0) revealed a poor or negligible response at RT. Interestingly, the formation of composites between ZnO and SWCNT led to the synergetic effect. The response level increased by deposition of ZnO while showing the maximum response with ZC30. Further deposition of ZnO to the composite, ZC60, degraded the response. ZC90 and ZC120 composites with further thicker deposition even changed the polarity of the response, i.e. p-type to *n*-type sensing [11,21,41,42]. Such trend is similarly observed in the elevated temperature. The ZnO-driven enhancement mechanism of the sensing performance can be elucidated by the conductance change under H_2 adsorption in the composites as discussed in the right panel of Fig. 6.

The temperature dependence of H_2 sensing performance in the p-type SWCNT (higher sensing response at lower temperature) confirms that the sensing of H_2 is enabled by H_2 adsorption given by [12,43]

$$H_2 \rightarrow 2H^+_{ad} + 2e^- \quad or \quad H_2 \rightarrow H^+_{2,ad} + e^- \tag{1}$$

Electrons released from adsorbed H_2 (or H) recombine with holes in the SWCNT, leading to the decrease of conductance that can be probed by the sensing signal. The charge exchange accompanied by the hydrogen adsorption results in the formation of the depletion region underneath the H_2 adsorption, as shown in Fig. 6**a**. The conductance modulation by the impingement of 500 ppm H_2 was ~ 12%, and it decreased at higher temperatures (Fig. 7b) due to higher probability of the desorption process. Meanwhile, pure ZnO revealed zero response to 500 ppm H_2 at RT (**Fig. S1h**), of which condition can be understood by Fig. 6**e**. The schematic model shows agglomerated ZnO nanoparticles with neutral cores and depleted surface due to oxygen ionsorption, thus ZnO shows an *n*-type conduction behavior. Since H_2 adsorption on the ZnO is negligible at RT, surface conditions of ZnO negligibly change with the hydrogen impingement, leading to zero response signal.

Based on the intrinsic properties of the SWCNT and ZnO towards H_2 molecules at RT, we can further discuss the enhancement mechanism of sensing ability in SWCNT/ZnO composite sensors. As discussed earlier, the response could be enhanced with deposition of ZnO nanoparticles on SWCNT while showing the maximum response of ~ 48% with ZC30 at RT (Fig. 7c). The left scheme of Fig. 6**b** presented the electron-depleted ZnO nanoparticle resulting from the contact with SWCNT in the standby condition. The question is how the increase of H_2 adsorption followed by more charge modulation can occur in SWCNT/ZnO composites. The improved response with ZnO deposition is attributed to the combined effect of the decrease in the conductance of SWCNT and the increase in the adsorption sites for H_2 at the interface. While the former was already proven by the conductance change due to the formation of pn-junction by ZnO addition (see the left panel of Fig. 6**b**), the latter is available through the contact interface between ZnO and SWCNT as assumed by the right scheme of Fig. 6**b**. As the number of ZnO particles in contact with the SWCNT further increases, the larger volume of pn-junctions leads to the decrease in the conductance of the SWCNT transducer, as shown in ZC30 (the left panel of Fig. 6**c**). At the same time, the H_2 adsorption sites also proportionally increase, leading to the complete depletion of SWCNT (Fig. 6**c** right). In such condition, the H_2 adsorption is limited by the hole concentration supplied from the SWCNT. The maximum response observed with ZC30

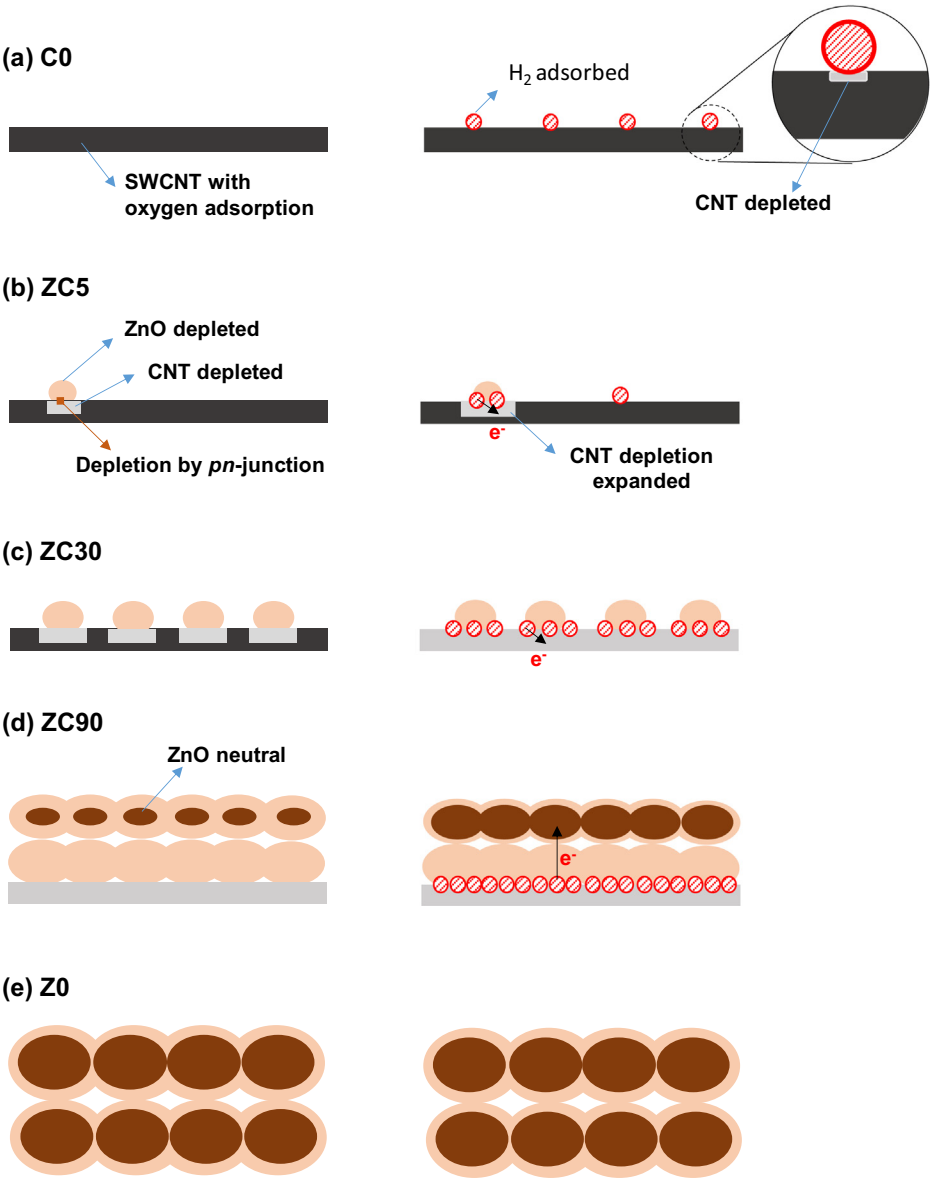

Fig. 6. Schematic presentation of the electronic sensor conditions before (left) and after (right) the hydrogen impingement at RT. (a) C0 or SWCNTs: adsorption of hydrogen molecules forms a hole depletion region in the SWCNT, but the consequent conductance change is small due to the limited H_2 adsorption sites on the SWCNT. (b) ZC5: small ZnO nanoparticles deposited on the SWCNT form pn-junctions and the depletion region in the SWCNT. The ZnO-SWCNT interface provides additional H_2 adsorption sites and the depletion in the SWCNT further expands by H_2 adsorption. (c) ZC30: ZnO-SWCNT interface and the pn-junction increase and the depletion volume in the SWCNT approaches towards the maximum. All the ZnO particles are depleted and the SWCNT still transport the current in the sensor. The electron released from H_2 adsorption goes to the SWCNT and increases its depletion. (d) ZC90: A thicker ZnO deposition with increasing particle size reaches the complete depletion of the SWCNTs while some ZnO particles form the neutral region providing the current transport path showing the *n*-type sensing behavior. Note the decreasing ZnO depletion with H_2 flow is based on the electron released from H_2 adsorption at the interface at RT. (e) Z0 of pure ZnO film: The largest ZnO particle size is developed. Since the ZnO particles does not adsorb H_2 at RT (**Fig. S1h**), there are no depletion region modulation leading to zero response.

could be achieved by the highest ratio of the conductance before and after the H_2 adsorption (or in the left and right of Fig. 6**c**). Namely, ZnO addition into SWNT-based sensors induced an increase in the number of available adsorption sites and a decrease in the initial conductance of the sensor, which comprised the maximum response in ZC30 (Fig. 7c).

With further ZnO deposition as in ZC90, the sensor revealed an *n*-type conduction behavior in its standby condition due to the oversupply of ZnO particles that are electronically separated from the SWCNT (the left panel of Fig. 6**d**). In this composite, SWCNT is completely depleted of the holes. In such condition, the electrons released from the H_2 adsorption at the SWCNT/ZnO interface are transferred to the excessive *n*-type ZnO nanoparticles (Fig. 6**d** right). This charge exchange process reveals the *n*-type sensor behaviour although the related response level was small at RT (**Fig. S1g**). In the extreme case of ZnO-rich condition, i.e. Z0 (pure ZnO), there are no adsorption sites for H_2 on ZnO thus the response level is negligible at RT as shown in **Fig. S1h** as well as in the right scheme of Fig. 6**e**.

To further investigate the sensing mechanism of the SWCNT-dominated sensors, the sensing property of ZC30 upon exposure to 500 ppm H_2 diluted in N_2 not dry air was measured at RT. The sensor was again heated at 350 °C for 1 h and then cooled down to room temperature in order to desorb all pre-adsorbed oxygen and water molecules. The response curve, **Fig. S2a**, showed a response of ~ 35% without oxygen in the environment and clearly confirmed the adsorption mechanism of Equation (1) for H_2 at RT. The response of ZC30 to 500 ppm NH_3 at various temperatures is

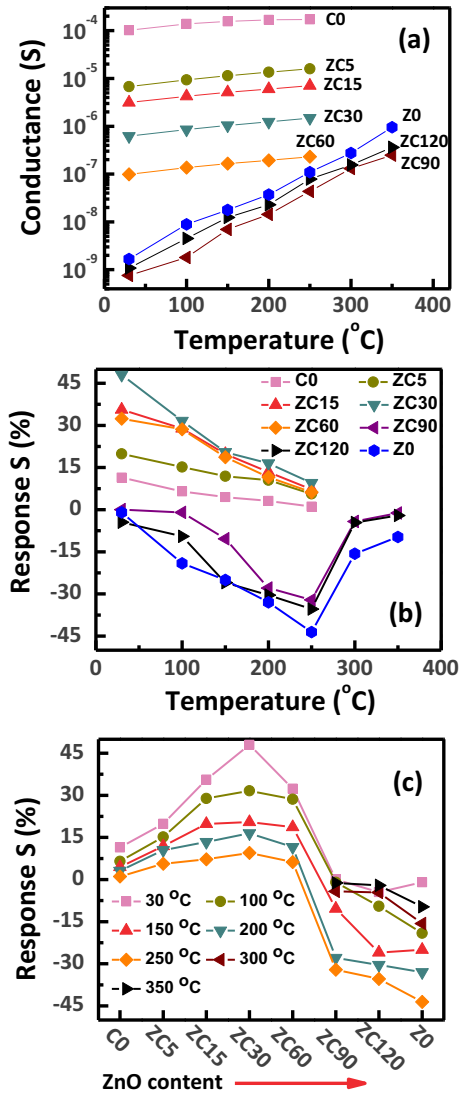

Fig. 7. (a) The conductance change in the sensors measured at different operating temperature. Sensing responses of the networked SWCNT/ZnO sensors toward 500 ppm H_2 as a function of (b) temperature and (c) ZnO contents.

also shown in **Fig. S2b**, which confirms that the SWCNT-dominated sensors, in general, show a high adsorption capability toward reducing gases such as H_2 and NH_3 at RT.

Of interesting note is that the SWCNT-dominated sensors show the decrease in the response level as the temperature increases (Fig. 7b-c). On the other hand, the ZnO-dominated sensors revealed the increase in responses as the temperature increases. This transition of temperature dependence in sensing performance is originated from the fundamentally different sensing mechanisms between SWCNT and ZnO. At room temperature, the SWCNT adsorb H_2 via Equation (1) while ZnO cannot adsorb H_2. On the contrary, at high temperature, the H_2 adsorption on the SWCNT surface and reaction with oxygen of the SWCNT are small (see the small response for C0 at 250 °C in Fig. 7c) while H_2 reacts dominantly with ionosorbed oxygen on ZnO (see the great response for Z0 at 250 °C in Fig. 7c). The latter combustion reaction mechanism at high temperatures is given by [44–46]:

$$H_2 + O_{ad}^- \rightarrow H_2O \uparrow + e^- \quad (2)$$

With the ZnO-dominated sensors with *n*-type transporting ZnO channel, the combustion reaction mechanism with ZnO for H_2 sensing is activated at high temperature leading to the relatively high responses as shown in Fig. 7b–c. Therefore, the maximum response was observed at 250 °C with pure ZnO (Z0), which indicates that composite formation with SWCNT does not result in any synergy effect for H_2 sensing at high temperature. However, in the SWCNT-dominated sensors with a small but finite numbers of ZnO nanoparticles, the surface combustion reaction led to an enhancement in the response compared with the SWCNT that did not show the response at high temperature. It again confirms our discussion that the electrons released from the combustion reaction on the ZnO particles are transferred to the SWCNT in the SWCNT/ZnO composites, exhibiting the p-type conduction.

Since ZC30 composite sensor showed the best room temperature performance, its sensing property was further investigated with various hydrogen gas concentrations in the range of 100–400 ppm at RT. As shown in Fig. 8a and the inset, a linear concentration dependence of the response could be observed, which confirms good linearity and reliability of the sensor. In addition, the repeatability of sensing examined for 0.1% H_2 concentration was studied (Fig. 8b). Finally, the selectivity of the sensor was also examined using various kinds of gases (Fig. 8c). The response to reducing gases of 500 ppm CH_4, CO, H_2S, NH_3, and H_2 were shown.

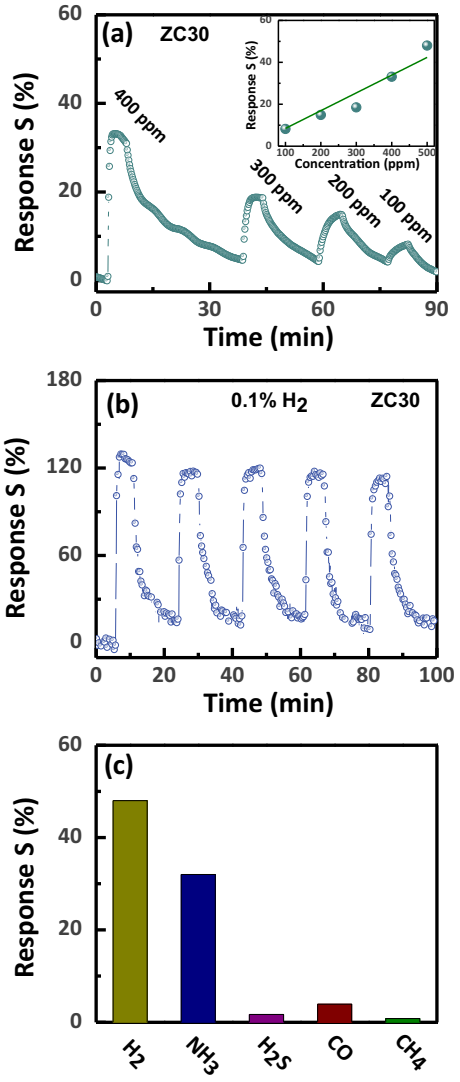

Fig. 8. (a) Sensing responses of the ZC30 sensor against various H_2 concentrations, showing a good linearity (inset). (b) Repeatability of the ZC30 sensor for 0.1% H_2 at 30 °C. (c) Comparison of the sensing responses for different gases (H_2, NH_3, H_2S, CO, and CH_4).

Our observations suggest that the SWCNT/ZnO composite could be employed for H_2 sensing and the pn-heterostructure can be used to achieve the high sensing performance.

The stability of sensing at room temperature in the humid environment, of which condition is similar to the human body, is important for the breath diagnosis sensor. To study the sensing stability against humidity, H_2 sensing behaviors of the ZC30, C0, and Z0 sensors were investigated in 50% relative humidity (RH) at RT and 200 °C (**Fig. S4**). The conductances measured at 0% RH and 50% RH, G_0 and G_{50}, respectively, and sensing responses are presented in Fig. 9. The conductance change caused by 50% RH was measured by $(G_0 - G_{50})/ G_0$, and it decreased by ~ 19% and ~ 6% for ZC30 at 30 °C and 200 °C, respectively, as shown in Fig. 9a. This result can be explained by the chemisorption of water molecules on the sensor surface. Water molecules suffered dissociation reaction into hydroxyl species followed by donation of electrons, which ultimately decrease conductivity in the p-type sensors [47,48]. The conductance and corresponding sensing response of pure SWCNT (C0) and ZnO (Z0) was also measured for the comparative studies. Decreases in the conductance was also observed for p-type C0 sensor, which were ~ 6% and ~ 2% at RT and 200 °C, respectively, as shown in Fig. 9b. On the other hand, the conductance of *n*-type Z0 sensor increased by exposure to 50% RH, which were ~ 372% and ~ 18% at RT and 200 °C, respectively (Fig. 9c). The results of conductance change observed were summarized in Fig. 9d.

The comparison of conductance clearly demonstrated the higher humidity effect at the lower temperature for both CNT and ZnO. All sensors are less affected by water adsorption at 200 °C. Of particular note is that the humidity effect on conductance is far higher with the surface of ZnO than with that of SWCNT at the given temperature, which is more prominent at RT. The humidity effect on the conductance is directly reflected to the difference in the response. As a result, the p-type C0 and ZC30 sensors showed relatively small difference in the response compared with Z0 sensor at both RT and 200 °C. Given that Z0 showed negligible responses to H_2 gas at RT, the conductance change by the humidity resulted in the great change in the conductance (Fig. 9d). Meanwhile, the exposure to the humidity led to a relatively large decrease in the response from 33% to 15% at 200 °C at which H_2 could react with the surface of ZnO.

All in all, the relatively weak humidity dependence of ZC30 was attributed to the SWCNT of small humidity effect and it is more prominent at RT. Since the considerable influence of humidity on metal oxides was observed in our previous studies as well [49,50], the stable sensing performance of the ZC30 composite sensor against humidity originated from the immunity of SWCNT to the water molecules. This relatively low humidity dependence can be another advantage of the SWCNT-dominated SWCNT/ZnO composite sensor for hydrogen detection from the human breath.

4. Conclusion

Networked ZnO/SWCNT composites were fabricated by the arc-discharge method and various contents of ZnO nanoparticles were incorporated by sputtering. The morphology, structure, electrical properties, and H_2 sensing performances of nanocomposites were thoroughly investigated at various temperatures. The ZnO/SWCNT nanocomposite responded to ppm levels of H_2 gas concentration and exhibited the highest response at room temperature. We scrutinized the effect of ZnO in the composite, by which different sensing mechanisms work in the SWCNT-dominated sensors and ZnO-dominated sensors. We elaborated the synergistic effect in the nanocomposite and proved that interactive function between the decrease in the conductance of the SWCNT *and* the enhanced adsorption of H_2 molecules accounted for the enhanced response in the composite sensor at RT. In addition, the stable operation of the sensor is also confirmed by linearity, selectivity, and reproducibility. Though the humidity effect was unavoidable at RT, more stable sensing properties under the humidity could be obtained in the ZC30 sensor by the less sensitivity of the SWCNT conductance to the adsorption of water molecules. While our study is the pioneering work to unveil the sensing mechanism in the pn-junction type nanocomposite sensor, we believe that our

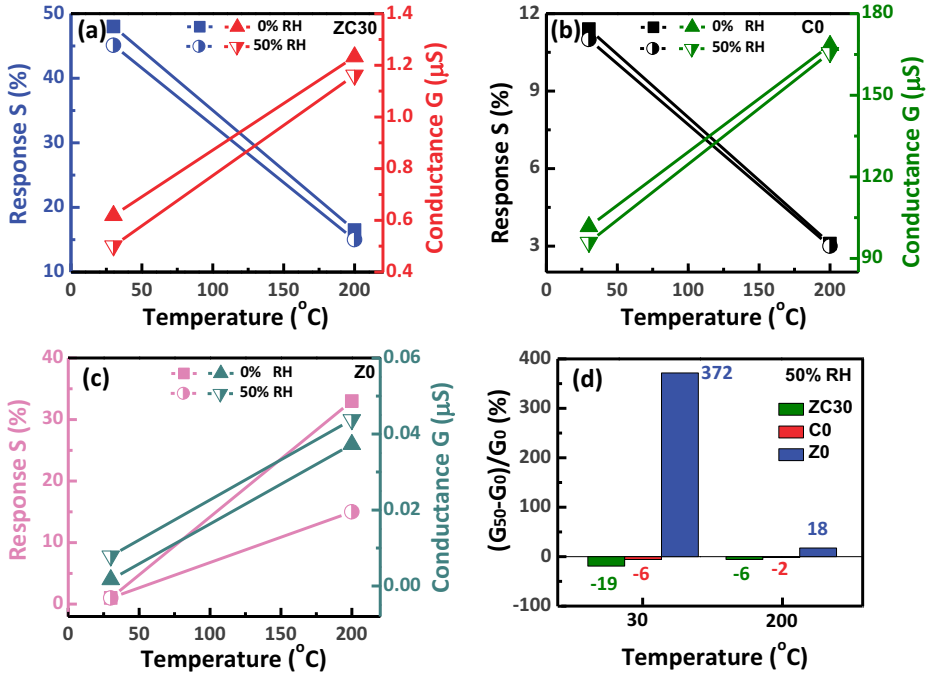

Fig. 9. Conductance and response to 500 ppm H_2 gases in two RH (0% and 50%) measured for the sensors (a) ZC30, (b) C0, and (c) Z0. Measurement results at two different sensor temperatures (30 °C and 200 °C) are compared for the humidity effect. (d) The conductance changes due to 50% RH measured by $(G_{50}-G_0)/G_0$ for the sensors at 30 °C and 200 °C.

nanocomposite sensor is one of the promising candidates for the hydrogen breath test, which can be easily integrated into a portable device with low power consumption.

Declaration of Competing Interest

The authors declare that they have no known competing financial interests or personal relationships that could have appeared to influence the work reported in this paper.

Acknowledgment

This work was supported by the National Research Lab program (2018R1A2A1A05023126) of the National Research Foundation of Korea.

Appendix A. Supplementary material

Supplementary data to this article can be found online at https://doi.org/10.1016/j.jcis.2020.10.017.

References

[1] S.M. Abbott, J.B. Elder, P. Španěl, D. Smith, Quantification of acetonitrile in exhaled breath and urinary headspace using selected ion flow tube mass spectrometry, Int. J. Mass Spectrom. 228 (2) (2003) 655–665.
[2] A.A.S. Amann, David, Breath Analysis for Clinical Diagnosis and Therapeutic Monitoring.
[3] K. Yan, D. Zhang, D. Wu, H. Wei, G. Lu, Design of a Breath Analysis System for Diabetes Screening and Blood Glucose Level Prediction, IEEE Trans. Biomed. Eng. 61 (11) (2014) 2787–2795.
[4] W. Cao, Y. Duan, Current Status of Methods and Techniques for Breath Analysis, Crit. Rev. Anal. Chem. 37 (1) (2007) 3–13.
[5] M. Phillips, J. Herrera, S. Krishnan, M. Zain, J. Greenberg, R.N. Cataneo, Variation in volatile organic compounds in the breath of normal humans, J. Chromatogr. B Biomed. Sci. Appl. 729 (1) (1999) 75–88.
[6] W. Miekisch, J.K. Schubert, G.F.E. Noeldge-Schomburg, Diagnostic potential of breath analysis—focus on volatile organic compounds, Clin. Chim. Acta 347 (1) (2004) 25–39.
[7] I. Ohsawa, M. Ishikawa, K. Takahashi, M. Watanabe, K. Nishimaki, K. Yamagata, K.-I. Katsura, Y. Katayama, S. Asoh, S. Ohta, Hydrogen acts as a therapeutic antioxidant by selectively reducing cytotoxic oxygen radicals, Nat. Med. 13 (2007) 688.
[8] M.D. Levitt, Production and Excretion of Hydrogen Gas in Man, N. Engl. J. Med. 281 (3) (1969) 122–127.
[9] G.L. Simon, S.L. Gorbach, Intestinal flora in health and disease, Gastroenterology 86 (1) (1984) 174–193.
[10] E. Alexander, A. Anton, S. Michael, D. Bettina, L. Maximilian, Implementation and interpretation of hydrogen breath tests, J. Breath Res. 2 (4) (2008) 046002.
[11] H.F. Hammer, Colonic hydrogen absorption: quantification of its effect on hydrogen accumulation caused by bacterial fermentation of carbohydrates, Gut 34 (6) (1993) 818.
[12] J. Kong, N.R. Franklin, C. Zhou, M.G. Chapline, S. Peng, K. Cho, H. Dai, Nanotube Molecular Wires as Chemical Sensors, Science 287 (5453) (2000) 622.
[13] P.G. Collins, K. Bradley, M. Ishigami, A. Zettl, Extreme Oxygen Sensitivity of Electronic Properties of Carbon Nanotubes, Science 287 (5459) (2000) 1801.
[14] J. Kong, H. Dai, Full and Modulated Chemical Gating of Individual Carbon Nanotubes by Organic Amine Compounds, J. Phys. Chem. B 105 (15) (2001) 2890–2893.
[15] K. Bradley, J.-C.-P. Gabriel, A. Star, G. Grüner, Short-channel effects in contact-passivated nanotube chemical sensors, Appl. Phys. Lett. 83 (18) (2003) 3821–3823.
[16] I. Sayago, E. Terrado, M. Aleixandre, M.C. Horrillo, M.J. Fernández, J. Lozano, E. Lafuente, W.K. Maser, A.M. Benito, M.T. Martinez, J. Gutiérrez, E. Muñoz, Novel selective sensors based on carbon nanotube films for hydrogen detection, Sens. Actuat. B 122 (1) (2007) 75–80.
[17] Y.-P. Sun, K. Fu, Y. Lin, W. Huang, Functionalized Carbon Nanotubes: Properties and Applications, Acc. Chem. Res. 35 (12) (2002) 1096–1104.
[18] A. Hirsch, Functionalization of Single-Walled Carbon Nanotubes, Angew. Chem. Int. Ed. 41 (11) (2002) 1853–1859.
[19] S. Mahouche Chergui, A. Ledebt, F. Mammeri, F. Herbst, B. Carbonnier, H. Ben Romdhane, M. Delamar, M.M. Chehimi, Hairy Carbon Nanotube@Nano-Pd Heterostructures: Design, Characterization, and Application in Suzuki C−C Coupling Reaction, Langmuir 26 (20) (2010) 16115–16121.
[20] N. Van Hieu, L.T.B. Thuy, N.D. Chien, Highly sensitive thin film NH3 gas sensor operating at room temperature based on SnO2/MWCNTs composite, Sens. Actuat. B 129 (2) (2008) 888–895.
[21] D.R. Miller, S.A. Akbar, P.A. Morris, Nanoscale metal oxide-based heterojunctions for gas sensing: A review, Sens. Actuat. B 204 (2014) 250–272.
[22] M. Mashock, K. Yu, S. Cui, S. Mao, G. Lu, J. Chen, Modulating Gas Sensing Properties of CuO Nanowires through Creation of Discrete Nanosized p–n Junctions on Their Surfaces, ACS Appl. Mater. Interf. 4 (8) (2012) 4192–4199.
[23] W. Hyung-Sik, N. Chan Woong, K. Il-Doo, L. Jong-Heun, Highly sensitive and selective trimethylamine sensor using one-dimensional ZnO–Cr 2 O 3 hetero-nanostructures, Nanotechnology 23 (24) (2012) 245501.
[24] S. Mridha, D. Basak, Investigation of a p-CuO/n-ZnO thin film heterojunction for H 2 gas-sensor applications, Semicond. Sci. Technol. 21 (7) (2006) 928.
[25] N.D. Chinh, N.D. Quang, H. Lee, T. Thi Hien, N.M. Hieu, D. Kim, C. Kim, D. Kim, NO gas sensing kinetics at room temperature under UV light irradiation of In2O3 nanostructures, Sci. Rep. 6 (2016) 35066.
[26] N.M. Vuong, D. Kim, H. Kim, Surface gas sensing kinetics of a WO3 nanowire sensor: part 1—oxidizing gases, Sens. Actuat. B 220 (2015) 932–941.
[27] N.D. Hoa, N. Van Quy, D. Kim, Nanowire structured SnOx–SWNT composites: High performance sensor for NOx detection, Sens. Actuat. B 142 (1) (2009) 253–259.
[28] T.I.T. Okpalugo, P. Papakonstantinou, H. Murphy, J. McLaughlin, N.M.D. Brown, High resolution XPS characterization of chemical functionalised MWCNTs and SWCNTs, Carbon 43 (1) (2005) 153–161.
[29] H.K. Jeong, E. Echeverria, P. Chakraborti, H.T. Le, P.A. Dowben, Electronic structure of cyclodextrin-carbon nanotube composite films, RSC Adv. 7 (18) (2017) 10968–10972.
[30] Z. Mi, L.P. Frank, A.D. Peter, B. Alex, S. Mathias, D. Vanya, Y. Rositza, K. Lingmei, A.K. Jeffry, Direct graphene growth on Co 3 O 4 (111) by molecular beam epitaxy, J. Phys. Condens. Matter 24 (7) (2012) 072201.
[31] X.Q. Wei, B.Y. Man, M. Liu, C.S. Xue, H.Z. Zhuang, C. Yang, Blue luminescent centers and microstructural evaluation by XPS and Raman in ZnO thin films annealed in vacuum, N2 and O2, Physica B 388 (1) (2007) 145–152.
[32] R. Al-Gaashani, S. Radiman, A.R. Daud, N. Tabet, Y. Al-Douri, XPS and optical studies of different morphologies of ZnO nanostructures prepared by microwave methods, Ceram. Int. 39 (3) (2013) 2283–2292.
[33] R. Cebulla, R. Wendt, K. Ellmer, Al-doped zinc oxide films deposited by simultaneous rf and dc excitation of a magnetron plasma: Relationships between plasma parameters and structural and electrical film properties, J. Appl. Phys. 83 (2) (1998) 1087–1095.
[34] S. Lefrant, I. Baltog, M. Baibarac, Surface-enhanced Raman scattering studies on chemically transformed carbon nanotube thin films, J. Raman Spectrosc. 36 (6–7) (2005) 676–698.
[35] M.S. Dresselhaus, G. Dresselhaus, A. Jorio, A.G. Souza Filho, R. Saito, Raman spectroscopy on isolated single wall carbon nanotubes, Carbon 40 (12) (2002) 2043–2061.
[36] A. Jorio, M.A. Pimenta, A.G.S. Filho, R. Saito, G. Dresselhaus, M.S. Dresselhaus, Characterizing carbon nanotube samples with resonance Raman scattering, New J. Phys. 5 (1) (2003) 139.
[37] L.-C. Wang, K.-T. Tang, I.J. Teng, C.-T. Kuo, C.-L. Ho, H.-W. Kuo, T.-H. Su, S.-R. Yang, G.-N. Shi, C.-P. Chang, A Single-Walled Carbon Nanotube Network Gas Sensing Device, Sensors (Basel, Switzerland) 11 (8) (2011) 7763–7772.
[38] Y. Wang, J.T.W. Yeow, A Review of Carbon Nanotubes-Based Gas Sensors, J. Sens. 2009 (2009) 24.
[39] B. Arash, Q. Wang, Detection of gas atoms with carbon nanotubes, Sci. Rep. 3 (2013) 1782.
[40] V. Srikant, D.R. Clarke, On the optical band gap of zinc oxide, J. Appl. Phys. 83 (10) (1998) 5447–5451.
[41] I. Kosc, I. Hotovy, V. Rehacek, R. Griesseler, M. Predanocy, M. Wilke, L. Spiess, Sputtered TiO2 thin films with NiO additives for hydrogen detection, Appl. Surf. Sci. 269 (2013) 110–115.
[42] H. Huang, H. Gong, C.L. Chow, J. Guo, T.J. White, M.S. Tse, O.K. Tan, Low-Temperature Growth of SnO2 Nanorod Arrays and Tunable n–p–n Sensing Response of a ZnO/SnO2 Heterojunction for Exclusive Hydrogen Sensors, Adv. Funct. Mater. 21 (14) (2011) 2680–2686.
[43] L. Hu, D.S. Hecht, G. Grüner, Carbon Nanotube Thin Films: Fabrication, Properties, and Applications, Chem. Rev. 110 (10) (2010) 5790–5844.
[44] K. J., C.M. G., D. H., Functionalized Carbon Nanotubes for Molecular Hydrogen Sensors, Advanced Materials 13(18) (2001) 1384-1386.
[45] J.J. L., B. Ashkan, P.S. J., U. Ant, Hydrogen Sensing Using Pd-Functionalized Multi-Layer Graphene Nanoribbon Networks, Advanced Materials 22(43) (2010) 4877-4880.
[46] T. Hübert, L. Boon-Brett, G. Black, U. Banach, Hydrogen sensors – A review, Sens. Actuators, B 157 (2) (2011) 329–352.
[47] G. Heiland, D. Kohl, Physical and Chemical Aspects of Oxidic Semiconductor Gas Sensors A2 - SEIYAMA, Chemical Sensor Technology, Elsevier, Amsterdam, Tetsuro, 1988, pp. 15–38.
[48] Z. Bai, C. Xie, M. Hu, S. Zhang, D. Zeng, Effect of humidity on the gas sensing property of the tetrapod-shaped ZnO nanopowder sensor, Mater. Sci. Eng. B 149 (1) (2008) 12–17.
[49] N.D. Chinh, C. Kim, D. Kim, UV-light-activated H2S gas sensing by a TiO2 nanoparticulate thin film at room temperature, J. Alloy. Compd. 778 (2019) 247–255.
[50] N.D. Chinh, T.T. Hien, L. Do Van, N.M. Hieu, N.D. Quang, S.-M. Lee, C. Kim, D. Kim, Adsorption/desorption kinetics of nitric oxide on zinc oxide nano film sensor enhanced by light irradiation and gold-nanoparticles decoration, Sens. Actuat. B 281 (2019) 262–272.